

# PRISM: Phase-enhanced Radial-based Image Signature Mapping framework for fingerprinting AI-generated images

Emanuele Ricco<sup>1</sup>, Elia Onofri<sup>2</sup>, Lorenzo Cima<sup>3</sup>, Stefano Cresci<sup>3</sup>, Roberto Di Pietro<sup>1</sup>

<sup>1</sup> King-Abdullah University of Science and Technology (KAUST), CEMSE division, Thuwal, Saudi Arabia

<sup>2</sup> Institute for Applied Mathematics, National Research Council (IAC-CNR), Italy

<sup>3</sup> IIT-CNR, Pisa, Italy

name.surname@kaust.edu.sa, name.surname@iit.cnr.it, elia.onofri@iac.cnr.it

## Abstract

A critical need has emerged for generative AI: attribution methods. That is, solutions that can identify the model originating AI-generated content. This feature, generally relevant in multimodal applications, is especially sensitive in commercial settings where users subscribe to paid proprietary services and expect guarantees about the source of the content they receive. To address these issues, we introduce PRISM, a scalable Phase-enhanced Radial-based Image Signature Mapping framework for fingerprinting AI-generated images. PRISM is based on a radial reduction of the discrete Fourier transform that leverages amplitude and phase information to capture model-specific signatures. The output of the above process is subsequently clustered via linear discriminant analysis to achieve reliable model attribution in diverse settings, even if the model’s internal details are inaccessible. To support our work, we construct PRISM-36K, a novel dataset of 36,000 images generated by six text-to-image GAN- and diffusion-based models. On this dataset, PRISM achieves an attribution *accuracy* of 92.04%. We additionally evaluate our method on four benchmarks from the literature, reaching an average *accuracy* of 81.60%. Finally, we evaluate our methodology also in the binary task of detecting *real* vs *fake* images, achieving an average *accuracy* of 88.41%. We obtain our best result on GenImage with an *accuracy* of 95.06%, whereas the original benchmark achieved 82.20%. Our results demonstrate the effectiveness of frequency-domain fingerprinting for cross-architecture and cross-dataset model attribution, offering a viable solution for enforcing accountability and trust in generative AI systems.

## 1 Introduction

In recent years, generative Artificial Intelligence (AI) has experienced an unprecedented surge, becoming a foundational pillar of modern computing. Powered by advances in deep learning and the surge in computing capabilities, these systems can generate fluent text, realistic images, synthetic speeches, and even coordinate cross-modal reasoning tasks with increasing human-like coherence (Cao et al. 2023). The rapid adoption of generative AI technologies in both industry and society reflects their transformative potential. Multi-modal AI, in particular, unlocks new frontiers by seamlessly



Figure 1: Problem overview: users want assurance that the responses they receive originate from the specific model they have subscribed to.

integrating vision, language, and audio understanding, enabling more natural and context-rich human-computer interactions (Zhan et al. 2023). While the benefits are relevant and immediate, the fast-paced integration of generative AI raises important security and trust concerns that must be addressed with an adequate level of rigour and formalism, preserving applicability.

As generative AI is increasingly deployed in real-world social contexts, understanding its strengths and vulnerabilities has become a societal necessity to ensure its safe use (Pasupuleti, Vadapalli, and Mader 2023; Cima et al. 2025). A fundamental step is understanding the distinct characteristics of the generated artefacts, as this bears important practical implications. For example, by systematically analysing how different model configurations –such as architecture, size, training data, and decoding strategies–influence output features, it is possible to identify specific patterns that can serve as reliable signatures of the generated artifacts (Wißmann et al. 2024; Xu, Zhang, and Shi 2025). In turn, this can enable model fingerprinting, surpassing the binary task of *real* vs *fake* detection (Coccocini et al. 2024; Sha et al. 2024; Tan et al. 2024). Assessing the authenticity (*i.e.*, fingerprinting) of the source model that generated an artefact is both theoretically and practically important. Theoretically, since the black-box nature of large-scale generative models trades off performance for transparency (Cao et al. 2023). Practically, because the need for output-level fingerprinting is growing, especially in scenarios where commercial (*i.e.*, premium) APIs provide access to proprietary models (Ramesh et al. 2022a). Indeed,

as shown in Figure 1, end users may seek assurance that the generated artefacts they receive actually originate from the model they subscribed to, rather than from a—likely cheap—different one (Wißmann et al. 2024).

In this work, we move beyond the traditional binary distinction between human- and AI-generated content by tackling the challenging task of fingerprinting multiple models in the context of image generation (Wang et al. 2023). Specifically, given an image and a set of possible sources (either natural images or AI-generated), we aim at identifying the model that generated the image.

To this end, we introduce PRISM, a novel fingerprinting framework leveraging both the amplitude and phase components of the radial-reduced Discrete Fourier Transform (DFT) to capture subtle, yet informative, model-specific characteristics. Model attribution is then obtained with a supervised clustering step via Linear Discriminant Analysis (LDA). To validate PRISM, we create and publish a reference dataset of 36,000 images generated by six models, based on either GAN or diffusion architectures, from 40 distinct textual prompts. We evaluate PRISM on this dataset and on four additional reference datasets, achieving excellent and generalizable results. Our results underscore the potential of frequency-domain fingerprinting as a robust solution for model attribution, an essential step toward ensuring accountability, trust, and provenance in real-world deployments of generative AI systems.

**Contributions** Our contributions related to AI-generated image fingerprinting can be summarised as follows:

- We propose PRISM, a model-agnostic LDA-based framework that, exploiting radially-reduced frequency-domain features, accurately fingerprints AI-generated images to identify their source models.
- We generate and release PRISM-36K, a novel dataset of 36,000 images generated by six text-to-image (T2I) models, including both open-source and closed models.
- We evaluate our methodology across PRISM-36K and four publicly available benchmarks, achieving attribution accuracies of 92.0% on our dataset and between 76.3% and 88.5% on the existing ones.
- We further evaluate PRISM on the binary task of detecting *real* vs *fake* images, achieving an average accuracy of 88.41% and demonstrating its suitability in this task.
- We release both data and code,<sup>1</sup> to allow full reproducibility of our results.

## 2 Related Work

In the last few years, the content generated by AI has led to the flowering of many techniques to distinguish real from artifact data, due to the introduction of many techniques for image generation. The theme of model-specific fingerprinting is crucial for many reasons, such as intellectual property rights to ensure users comply with their legal licenses, as investigated in (Xu et al. 2024).

<sup>1</sup>A reduced version is available at: <https://shorturl.at/BBl0m>

The rapid advancement and widespread deployment of LLMs highlight the growing need for robust model attribution techniques, which are essential for identifying the source model and mitigating adversarial misuse. A commonly explored strategy involves watermarking generated outputs, *e.g.* embedding patterns through neutral token sequences (Kirchenbauer et al. 2023) or leveraging a powerful LLM, such as ChatGPT, to watermark outputs produced by other models (Zhong, Dasgupta, and Tanvir 2024). More recently, attention was also drawn to model fingerprinting not requiring the need for explicit watermarking.

In the textual domain, various approaches have emerged: to cite a few, in (Zeng et al. 2024) the authors leverage architectural patterns in transformers to identify three unique terms that distinguish base models, while (Alhazbi et al. 2025) propose a method based on timing intervals between token generations. Other efforts explore implicit markers (Wanli, Yiming et al. 2025), the scalability of fingerprinting techniques (Nasery et al. 2025), and the robustness against model merging (Yamabe et al. 2024). However, these fingerprinting approaches are focused exclusively on text-based LLMs.

Attributing AI-generated images to their source models has been a concern since the early days of GANs. Initial work showed that minor differences in architecture could leave identifiable output fingerprints (Yu, Davis, and Fritz 2019), prompting studies on how model structure shapes these patterns (Marra et al. 2019). A common approach involves embedding watermarks in training data to test their robustness against output perturbations (Yu et al. 2021). The rise of diffusion models has intensified interest in tracking image provenance (Ho, Jain, and Abbeel 2020). Techniques include injecting frequency-domain patterns into noise inputs (Wen et al. 2023) or embedding signatures directly into model weights (Fernandez et al. 2023). Other strategies use latent fingerprinting or user-specific digital signatures for accountability (Nie et al. 2023; Kim et al. 2024).

However, these approaches rely on low-level access to the model’s architecture or parameters—an assumption that does not hold for commercial platforms such as Midjourney or DALL-E 2, where internal details remain undisclosed. To overcome this limitation, we introduce a scalable, model-agnostic fingerprinting framework that operates without requiring access to proprietary internals. Unlike previous work that focuses mainly on distinguishing between different versions of the same model (Wißmann et al. 2024), our method tackles a distinct and novel task by attributing outputs to entirely different model families. A detailed comparison with other model-agnostic techniques is available in Appendix A, Table 3.

## 3 Datasets for Model Attribution

We consider an image as its split in RGB channels, namely a triplet of matrices in  $\{0, \dots, 255\}^{n_y \times n_x}$ , where  $n_x$  and  $n_y$  represent the bit-size of the image, obtained as the actual size multiplied by the image resolution. Formally, the set of all possible images is given by  $\mathcal{I} = \bigcup_{n_x, n_y \in \mathbb{N}} (\mathbb{N}_{256}^{n_y \times n_x})^3$ . Then, let  $\mathcal{X}$  be a set of  $N$  images generated by a set  $\mathcal{M}$  of



Figure 2: Example of images generated by the six different models forming PRISM-36K with the same prompt.

$M$  models. We define a dataset for the attribution task as the couple  $\mathcal{D} = (\mathcal{X}, \mathcal{Y})$ , where  $y_i \in \mathcal{Y}$  is the source of the image  $x_i \in \mathcal{X}$ , with  $x_i \in \mathcal{I}$ ,  $y_i \in \mathcal{M}$ .

Many datasets with generated images are available in the literature. However, these are often built for purposes such as fake image detection, visual quality evaluation, and identity preservation, and are therefore not suitable to be directly used for the model attribution task. For this reason, we first created a dataset specifically designed for this task.

### 3.1 PRISM-36K

We built PRISM-36K to serve as a reference benchmark for the model attribution task<sup>2</sup>. It comprises 36,000  $512 \times 512$  PNG images generated using six different T2I models selected based on the availability of open-access white papers. This ensures transparency, reproducibility, and the possibility of future extensions. Figure 2 shows examples of the images generated by the different models for the same prompt. Appendix Table 5 thoroughly reports the characteristics of each model included in the dataset. In particular, we considered the image resolution capabilities, underlying architecture (e.g., GANs (Reed et al. 2016), Transformers (Ding et al. 2021; Yu et al. 2022), Diffusion Models (Ho, Jain, and Abbeel 2020), CLIP (Radford et al. 2021)), and openness of their implementations. For instance, Stable Diffusion v1.4 is fully open (code, architecture, and weights available under a permissive license), while models such as VQGAN-CLIP and FuseDream are only partially open due to dependencies on proprietary components like CLIP. Conversely, PIXART- $\alpha$  and SANA are both released on GitHub under MIT and Apache 2.0 licenses respectively, yet being partially open as it is not possible to directly download the pre-trained weights. Finally, DALL-E 2 is the only closed model used, being accessible through paid APIs only.

To construct the dataset, we crafted a set  $\mathcal{P}$  of 40 prompts (see Appendix B) grouped into two categories: 20 short ( $p_1, \dots, p_{20}$ ) and 20 long ( $p_{21}, \dots, p_{40}$ ). Short prompts  $p_i$  follow a simple [subject-verb-complement] syntax, while corresponding long prompts  $p_{i+20}$  introduce additional contextual complexity over the short ones. Each prompt was used to generate 150 images per model, resulting in 6,000 images per model. Prompts were treated as auxiliary classes

for dataset split purposes, with the aim of learning discriminative features ascribable to the generation source only while being prompt-agnostic.

We also evaluated a carefully crafted *average* split in training vs. test set (80:20), so that short-long couples are preserved, *i.e.*, namely,  $(p_i, p_{i+20})$  are always paired in the same set, fostering the resulting model to foresee generalisation to previously unseen prompts. Here, “average” refers to the split being cherry-picked to obtain as-average-as-possible results w.r.t. possible splits, instead of taking the one maximising, say, *accuracy* (see later Section 5).

### 3.2 Literature Datasets

To benchmark our approach and ensure comparability with prior work, we applied our methodology to several publicly available datasets. In particular, we selected four open-access datasets presenting published white-papers on their construction, namely: Generated Faces in the Wild (GFW) (Borji 2022), DeepGuardDB (Namani et al. 2025), SuSy (Bernabeu-Perez, Lopez-Cuena, and Garcia-Gasulla 2024), and GenImage (Zhu et al. 2023) (for this latter one, we used its tiny version instead<sup>3</sup>).

Details and statistics of each dataset are summarised in Appendix A within Table 4, including image sources, format, resolution (being mostly varying across and within datasets), dataset size, and reported classes (typically *real* and *fake*). Along with real images (taken from COCO or unpublished sources), notably a total of 16 different AI sources are present, namely: DALL-E (v2, v3), Midjourney (original, tti, img), Stable Diffusion (v1.4, v1.5, v1.x, v3.0), GLIDE, IMAGEN, SDXL ABM, BiGGAN, VQDM, Wukong. It is also worth noticing that both DeepGuardDB and GenImage organise images as couples, where *fake* images are generated based on *real* ones.

## 4 Methodology

We now present the fundamental components of our proposed methodology, composed of an image magnitude-and-phase feature extraction through a radially-reduced DFT of the RGB channels, and the usage of LDA both as a dimensionality reduction and classification algorithm (see Figure 3). DFT, in fact, has been previously employed in the literature for frequency-based deepfake detection (Karageorgiou et al. 2025) and artefact analysis in generated images (Tan et al. 2024; Li et al. 2025), with the latter also incorporating phase information with the amplitude to enhance detection.

### 4.1 Feature Extraction and Analysis

Formally, we can define the “model attribution” problem as the task of training a discriminant function:

$$\begin{aligned} a: \mathcal{X} &\rightarrow \mathcal{M} \\ x &\mapsto m \end{aligned}, \tag{1}$$

mapping a given image  $x$  to the corresponding source  $m$ . It is worth noting that (1) is a natural generalisation of the more renowned task of “fake detection” which reduces the

<sup>2</sup>A reduced version is available at: <https://shorturl.at/BBl0m>

<sup>3</sup><https://www.kaggle.com/datasets/yangsangtai/tiny-genimage>

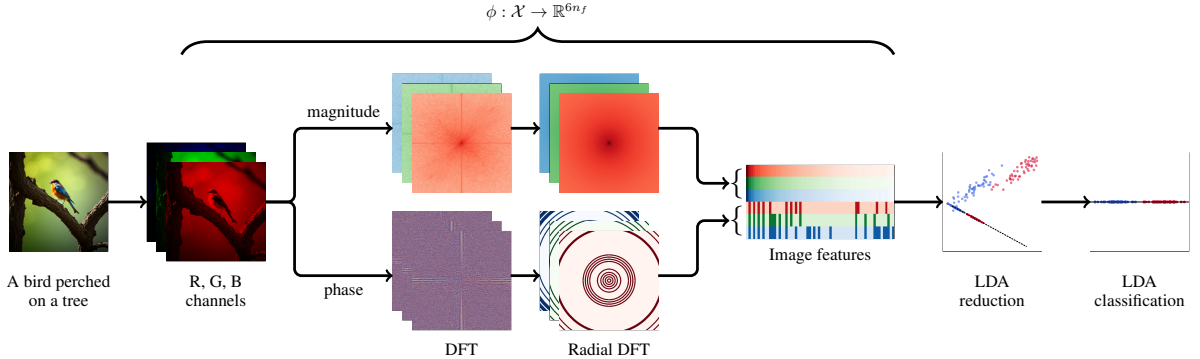


Figure 3: Overview of PRISM methodology. Given an image, feature extraction ( $\phi$ ) is applied prior to dimensionality reduction and classification with LDA.

sources space  $\mathcal{M}$  to the binary classification of *real* vs *fake*, and hence training a simpler function  $a_f : \mathcal{X} \rightarrow \{0, 1\}$ .

Due to the nature of our analysis, we decided to build our dataset in the lossless format of Portable Network Graphics (PNG), representing  $512 \times 512$  images directly as 3(4)  $512 \times 512$  matrices for the RGB(A) channels –the transparency layer A is constant 1 in our experiments and hence omitted. Moreover, we incorporated datasets from the literature containing images in the JPEG and WebP lossy formats.

Each colour channel is subsequently transformed into the frequency domain via a two-dimensional DFT, followed by frequency centralisation (see Appendix C for further reference). We then compute the corresponding radial profile –referred to as radial DFT (rDFT)– by averaging the spectral log-magnitude  $\bar{M}_{u,v}$  and phase  $\bar{\Phi}_{u,v}$  across  $n_r = 64$  evenly spaced annular region  $\mathcal{B}_1, \dots, \mathcal{B}_{n_r}$  spanning the frequency space. More in detail, for each bin  $i = 1, \dots, n_r$ , we compute the mean of the log-magnitude values and the cosine-transform of the circular mean of the phase angles as:

$$M_i = \frac{1}{|\mathcal{B}_i|} \sum_{(u,v) \in \mathcal{B}_i} \bar{M}_{u,v}, \quad (2)$$

$$\Phi_i = \cos \left( \arg \left( \frac{1}{|\mathcal{B}_i|} \sum_{(u,v) \in \mathcal{B}_i} e^{i\bar{\Phi}_{u,v}} \right) \right), \quad (3)$$

where the cosine-transform is used to identify  $-\pi$  and  $\pi$  angles without any potential loss of information (since the matrix is Hermitian, the aggregated phase collapses on  $\{0, \pi\}$ ). This yields a compact radial representation of both magnitude and phase spectra, while also standardising the approach w.r.t. the possible image dimensions  $n_x, n_y$  and fostering the resilience against different lossy formats.

The aggregated descriptors for each colour channel are finally concatenated into a feature vector  $\mathbf{f} \in \mathbb{R}^{6n_r}$ , later used in downstream analysis tasks. In what follows, we identify with  $\phi : \mathcal{X} \rightarrow \mathbb{R}^{6n_r}$  this procedure, as also depicted in Figure 3. Figure 4 reports a few examples of such vectors for the various models considered in our analysis, along with the average value of all images per model.

## 4.2 Model Attribution Pipeline

Let us consider our dataset  $\mathcal{D} = \{\mathcal{X}, \mathcal{Y}\}$  and let us denote with  $\mathcal{F} = \{\mathbf{f}_i\}_{i=1}^N$  the set of feature vectors  $\mathbf{f}_i \in \mathbb{R}^{6n_f}$  obtained as  $\mathbf{f}_i = \phi(x_i) \in \mathcal{X}$  through the rDFT feature extraction procedure described in Section 4.1 and normalised. As it is common in the literature, designing a discriminant function  $a$  (cf. Eq. (1)) mainly involves two distinct tasks:

- choosing a suitable dimensionality reduction  $\rho : \mathbb{R}^{6n_f} \rightarrow \mathbb{R}^{n_e}$ , for some reduced number of features  $n_e \leq 6n_f$ , to project the data into a more tractable embedding space;
- identifying a classification strategy  $\kappa : \mathbb{R}^{n_e} \rightarrow C$ , where  $C$  denotes a set of  $k \geq M$  clusters.

Particularly, when  $C = \mathcal{M}$ , then it is straightforward to compose  $\kappa$ , and  $\rho$  with the feature extractor  $\phi$  to create a valid discriminant function  $a$ :

$$a = \kappa \circ \rho \circ \phi \quad (4)$$

$$a : \mathcal{X} \rightarrow \mathbb{R}^{6n_f} \rightarrow \mathbb{R}^{n_e} \rightarrow \mathcal{M}$$

Amongst the many dimensionality reduction techniques available in the literature, we focus in particular on LDA (Zhao et al. 2024). In fact, unlike unsupervised techniques such as, e.g., PCA and t-SNE, LDA is a supervised method that explicitly incorporates class label information to optimise separability. In detail, LDA seeks a linear projection maximising class separability by the optimisation of the ratio between inter-class and intra-class variance. This results in a  $M - 1$  dimensional embedding where clusters (now interpreted as known classes) are optimally separated, naturally aligning dimensionality reduction with classification. In fact, along with the inherent dimensionality reduction offered by the embedding, LDA also admits a generative probabilistic interpretation, where each class is modelled as a Gaussian distribution with shared covariance; in this predictive formulation, it can be directly used as a classifier without requiring an additional clustering step (actually directly merging  $\rho$  and  $\kappa$  contributions).

## 4.3 Evaluating the Results

Upon defining the attribution pipeline via the supervised discriminant function (4), the final step consists of selecting appropriate performance indicators. Given the semi-supervised

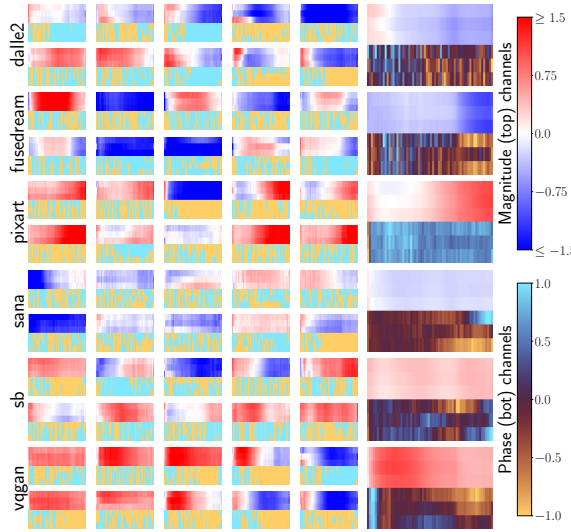


Figure 4: Examples of model fingerprints. Each small box represents the features extracted from a single generated image, with the upper half displaying the Fourier log magnitude (normalised) and the lower half showing the corresponding cosine-transformed phase. Each rightmost (big) box illustrates the average spectrum for the corresponding AI model, built as the median magnitude and the average phase spectra within all the model samples.

nature of the proposed approach, we adopt four classical classification metrics (*accuracy*, *precision*, *recall* and  $F_1$ -*score*), all computed in their weighted form to account for the multi-class nature of the problem.

To ensure a robust evaluation and mitigate randomness in dataset splits, we computed all scores over  $N_s$  randomly sampled 80:20 train-test partitions, while preserving the different prompts (*i.e.* 16 vs. 4 couples of prompts per split), hence guaranteeing prompt generalisation. This repeated evaluation serves a dual purpose: it provides an aggregated view of the typical performance in different close-to-random test conditions and supports the assessment of the method’s generalisation capabilities to unseen data.

In addition, we designate one reference split –selected as the one whose performance is closest to the mean across all splits– as the “average” split. This allows for a fair, standardised comparison among different methods or configurations, and provides a concrete instance on which to present detailed performance insights.

## 5 Results

In what follows, we firstly present the averaged results obtained from  $N_s = 1000$  different PRISM-36K random splits and we briefly analyse the relevance of the extracted features. Then, we present the results for the average split, selected as the most representative within the  $N_s$  we generated. Finally, we report the results obtained on the benchmark reference datasets introduced in Section 3.2.

We run all the experiments under Python 3.12.9 with scikit-learn 1.6.1 on an Intel Xeon W7-3465X worksta-

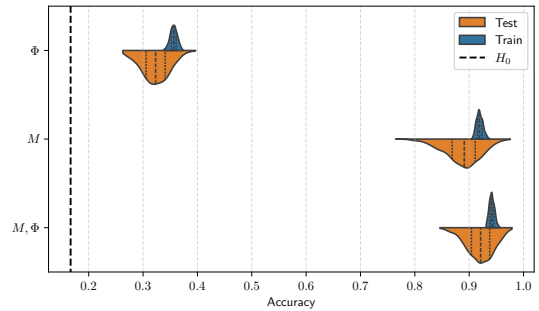


Figure 5: Distribution of test and training *accuracies* over  $N_s = 1000$  random splits. The usage of all the features is compared with the sole Phase ( $\Phi$ ) and the sole Magnitude ( $M$ ). The dashed black line represents the Null hypothesis ( $H_0$ ) where the class is randomly guessed.

tion equipped with 28/56 CPU threads (4.8 GHz) and 1 TB RAM, and repeated the tests for the sake of comparison on a MacBook Pro M3 Max Laptop, equipped with 16 CPU threads (4.05/2.75 GHz) and 64GB RAM. The Ubuntu 24.04 workstation swiftly handled the feature extraction on PRISM-36K, yielding 384 features for each of the 36K images in  $\sim 1$  h (110.59 MB memory usage). The radial reduction proved to be necessary, both for standardising the feature size (regardless the image original dimension) and for computational viability. Indeed, the extraction with the sole DFT yielded a dataset of 452.98 GB with 1,572,864 features per image ( $\sim 20$  min). Using the radial reduction, the Apple laptop executed the extraction in a comparable time of 94ms per image and completed the training phase on average in less than a second (0.89 s), achieving negligible test time.

### 5.1 Results on PRISM-36K

We start presenting the results of the training/test statistics over  $N_s = 1000$  splits of the datasets while preserving prompt separation, meaning that a couple of short-long prompts either appear in training or test set, but not both, actually ensuring correct prompt generalisation. In particular, with average *accuracy* being  $92.04 \pm 2.43$  (5–95% being 87.88–95.85, best results 97.89%), and comparable aggregated  $F_1$ -*score* (up to 0.1%), the method proved being robust and informative. Figure 5 reports the distribution of the *accuracies* within the  $N_s$  random splits, comparing the results obtained using both Magnitude and Phase ( $M, \Phi$ ) with the sole Magnitude ( $M$ ), the sole Phase ( $\Phi$ ), and the random guess ( $H_0$ ). It can be seen that, despite the phase being insufficient on its own to train a discriminator, combined features still offer a sensible advantage over the sole magnitude. The adoption of phase significantly increases ( $p \ll 10^{-10}$  under paired *t*-test) the mean *accuracy* by 3.23%, while also reducing the standard deviation by 25.64% –a marked and consistent improvement.

Upon selecting the split achieving the closest results (min sum of squared errors) to the average *accuracy*/ $F_1$ -*score*, *i.e.* the reference split, we present the corresponding confusion matrix in Figure 6, highlighting an overall *accuracy* of

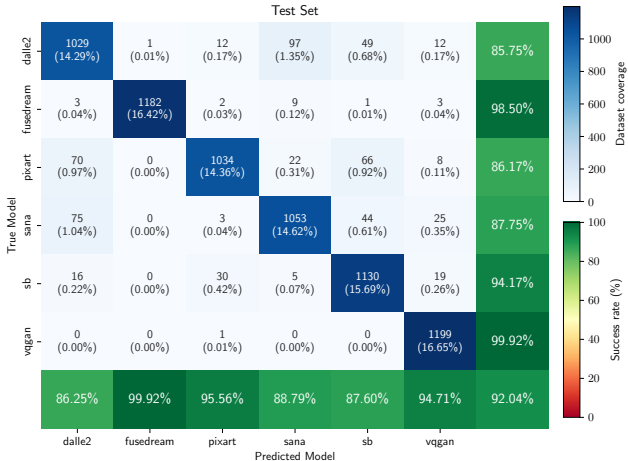


Figure 6: Confusion matrix of model predictions on the PRISM-36K test set. The last (external) row and column show model-wise *precision* and *recall* respectively, while their intersection represents the global *accuracy*.

92.04% (in line with the mean *accuracy*). Out of the considered datasets, *FuseDream* receives the most accurate attributions, almost reaching perfection with a *F<sub>1</sub>-score* of 0.99 (1182 correct, 18 false negatives, 1 false positive), followed closely by *VQGAN-CLIP* at 0.97% (suffering from a weaker *precision* despite the high *recall* of a single false negative). These results show that the proposed approach successfully learned highly discriminative features for these models. *PIXART- $\alpha$*  and *Stable Diffusion* achieve strong performances as well, securing both a *F<sub>1</sub>-score* of 0.91, the first due to high *precision* (95.56%) and the latter due to high *recall* (94.17%). Finally, *SANA* and *DALL-E 2* offer the most challenging models to discriminate, jeopardising the overall score with less brilliant statistics, actually achieving balanced *F<sub>1</sub>-scores* of 0.88 and 0.86, respectively. The *precision* and *recall* scores –corresponding respectively to the bottom row and right-most column of Figure 6– are however consistently high across all models, with no particular criticalities. The confusion patterns are minimal (575 misclassifications out of 7200), with most occurring between *DALL-E 2* and *SANA* which result mildly blended, accounting for 172 out of the total 575 misclassifications ( $\sim 30\%$ , distributed as 97 and 75, respectively). *Stable Diffusion* is also frequently misclassified (27.65% of the errors) in place of *PIXART- $\alpha$* , *DALL-E 2*, or *SANA*, probably being ascribable to the shared architecture all these models are built onto (cf. Appendix A – Table 5).

## 5.2 LDA Results on Reference Datasets

After evaluating our approach on PRISM-36K, we applied it to the other datasets presented in Section 3.2, obtaining both the results shown in Table 1 and in the boxplot represented in Figure 7. While the latter shows the distribution of the results obtained on  $N_s = 1000$  splits of each dataset, Table 1 compares the results achieved on the average split of our dataset with the results obtained on the

Table 1: Model attribution results.

Dataset	Models	Train/Test	Accuracy	<i>F<sub>1</sub>-score</i>
PRISM-36K	6	28.8k/7.2k	92.04	92.02
GenImage	8	28k/7k	88.47	88.25
SuSy	6	14.5k/5.6k	84.12	84.00
GFW	4	60.8k/15.2k <sup>†</sup>	77.07	76.55
DeepGuardDB	5	10.4k/2.6k <sup>†</sup>	76.31	75.46

<sup>†</sup> Random 80/20% split. Others use published splits.

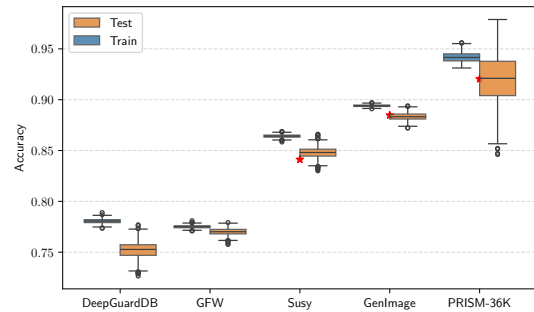


Figure 7: Performances boxplots (*accuracy*) on the five different datasets. *F<sub>1</sub>-score*, *precision*, and *recall* are nearly indistinguishable. Red star reports the values against the published split (cf. Table 1).

literature training-test splits for the *SuSy* and *GenImage* datasets and on random splits for the remaining datasets.

In detail, Table 1 shows that PRISM-36K is the most recognisable dataset, achieving the highest *accuracy* of 92.04% and *F<sub>1</sub>-score* of 92.02%; this is not surprising, considering that, conversely to the literature dataset, we have built it specifically to study the model attribution task. In contrast, DeepGuardDB and GFW represent the most challenging scenarios, with *accuracies* of 76.31% and 77.07% respectively, and corresponding *F<sub>1</sub>-scores* of 75.46% and 76.55%. The intermediate performance of GenImage (88.47% *accuracy*, 88.25% *F<sub>1</sub>-score*) and SuSy (84.12% *accuracy*, 84.00% *F<sub>1</sub>-score*) demonstrates that dataset composition and the specific generative models included significantly influence attribution capability.

The boxplot in Figure 7 reveals significant performance variations across the five datasets. Our dataset consistently performs better, showing *accuracies* concentrated around 90.40–93.78%, indicating excellent classification *accuracy*; however, major variance is obtained in *Test accuracy*, actually suggesting some prompts might be correlated, further enhancing performances when considered split within training and test set. GenImage and SuSy datasets show moderate performance with *accuracies* ranging around 88.10–88.59% and 84.45–85.13% respectively, while GFW and DeepGuardDB perform considerably lower, with results localising around 76.80–77.24% and 74.69–75.73%. The lower performance on DeepGuardDB can likely be attributed to the presence of lossy compression formats (JPEG, WebP) degrading the frequency-domain signatures.

Finally, results presented in Table 2 show the scores of our approach when used for distinguishing between real

Table 2: Results achieved on the binary classification task of *real vs fake* image detection.

Dataset	Paper	Train/Test	Accuracy	$F_1$ -score
GenImage	(Zhu et al. 2023)	28k/7k	82.20	-
	Ours	28k/7k	95.06	95.05
SuSy	Ours	14.5k/5.6k	95.01	95.03
GFW	Ours	60.8k/15.2k <sup>†</sup>	82.94	83.10
DeepGuardDB	(Namani et al. 2025)	10k/3k	99.87	-
	Ours	10.4k/2.6k <sup>†</sup>	81.62	81.41

<sup>†</sup> Random 80/20% split. Others use published splits.

and synthetic images across the four established reference datasets. The results, obtained without retraining for the specific task, demonstrate substantial variability in classification performance across datasets. *Accuracy* is overall higher w.r.t. the model attribution task, further suggesting the model attribution task being a generalisation of the *real vs fake* one. More in detail, GenImage achieved the highest overall performance with an *accuracy* (and  $F_1$ -*score*) of 95.0%, better than the performance achieved in the dataset reference paper (Zhu et al. 2023). Similarly, our approach performs well on SuSy, yielding the same performance as per GenImage (95.0%). In contrast, as before, GFW and DeepGuardDB exhibited more modest performance levels, with *accuracies* of 82.94% and 81.62%, and  $F_1$ -*scores* of 83.10% and 81.41% respectively.

## 6 Discussion

Our experiments confirm the effectiveness of frequency-domain fingerprinting for model attribution of AI-generated images in black-box conditions. The combination of magnitude and phase embeddings enables the extraction of structured spectral cues that are distinctive across generative models. The LDA-based classification pipeline achieves a strong average *accuracy* of 92.04% over 1000 random splits on PRISM-36K, peaking at 97.89% in favourable cases. Certain models exhibit unique and stable spectral signatures. For instance, FuseDream and VQGAN-CLIP consistently produce fingerprints that are highly separable, with  $F_1$ -*score* values of 99% and 97% respectively, suggesting the presence of stable and model-specific spectral biases likely rooted in the architectures or training procedures (Li et al. 2025; Giorgi et al. 2025). Conversely, models built on similar diffusion frameworks –such as Stable Diffusion and DALL-E 2– yield more overlapping spectral signatures, with lower attribution performances (91% to 86%).

The characteristics of the evaluation datasets also play a decisive role. Our controlled PRISM-36K achieves the highest attribution scores, benefiting from a balanced and clean distribution of prompt-image pairs. In contrast, public datasets introduce challenges stemming from heterogeneity in data curation. GenImage performs robustly (88.47% *accuracy*), but suffers from severe class imbalance. SuSy remains moderately effective (84.12%), while GFW and DeepGuardDB are the most challenging datasets, with an *accuracy* of 77.07% and 76.31%, mainly ascribable to mixed resolutions, colour spaces, and lossy compression formats (JPEG, WebP). These artefacts substan-

tially degrade frequency-domain fidelity, making our approach to attribution more difficult. Nonetheless, we achieve the best results on GFW and a competitive performance on DeepGuardDB. This variability highlights the need for reproducible, standardised benchmarks for multi-class model attribution. Moreover, while most of the prior literature focuses on binary *real vs fake* detection (Tan et al. 2024), our results confirm that full model attribution is a significantly harder task. For example, our method achieves 95.06% *accuracy* on the binary classification task for GenImage, outperforming (Zhu et al. 2023) by a large margin (95.06% vs 82.20%), while performing at 88.47% on full attribution. This supports the conclusion that model attribution generalises and extends beyond the binary setting.

Finally, we note that model attribution may be impacted by semantic mismatches between prompts and generated content. Prior work (Ricco, Cima, and Di Pietro 2025) shows that generative artefacts and hallucinations can introduce spectral anomalies. These perturbations—whether due to prompt ambiguity or instability in the generative process—may reduce attribution *accuracy* by introducing noise in the extracted frequency representation.

In summary, our findings validate the utility of frequency-based fingerprinting for model attribution and show that linear classifiers, such as LDA, represent an effective solution in this setting. These results encourage further development of scalable, interpretable, and reproducible attribution pipelines that operate under realistic, black-box conditions.

## 7 Conclusions

We proposed PRISM, a novel methodology for fingerprinting AI-generated images based on frequency-domain representations. Our approach generalises the conventional *real vs fake* detection task into the more informative, yet challenging, model attribution problem. By extracting features from both the magnitude and the phase of the radially-reduced DFT, we manage to accurately distinguish generative sources via Linear Discriminant Analysis only relying on frequency-domain patterns.

To validate our methodology, we constructed PRISM-36K, a controlled dataset comprising 36,000 images from six prominent text-to-image models, each sampled with the same set of 40 prompts. In addition, we evaluated our approach on four public benchmark datasets to assess its robustness under real-world conditions. On PRISM-36K, our method achieves an average attribution *accuracy* of 92.0%, with performance peaking at 97.9% in favourable splits. On benchmark datasets we obtain competitive results, reaching up to 88.5% *accuracy* on GenImage for the attribution task, and outclassing the reference accuracy in *real vs fake* classification (95.1% against 82.2% from the literature), hence demonstrating resilience even under adverse compression and class imbalance.

These results demonstrate the viability of frequency-based fingerprinting for model attribution, confirming that meaningful spectral artefacts are embedded in AI-generated content. However, several research directions remain open. In future work, we plan to explore unsupervised clustering to extend applicability in low-supervision settings, experiment

with alternative dimensionality reduction to detect embedded structural relationships in spectral features, and investigate their interpretability to better understand how they relate to generative model behaviour.

## References

Alhazbi, S.; Hussain, A.; Olinger, G.; and Papadimitratos, P. 2025. Llms have rhythm: Fingerprinting large language models using inter-token times and network traffic analysis. *IEEE Open Journal of the Communications Society*.

Bernabeu-Perez, P.; Lopez-Cuena, E.; and Garcia-Gasulla, D. 2024. Present and Future Generalization of Synthetic Image Detectors. *CoRR*.

Borji, A. 2022. Generated faces in the wild: Quantitative comparison of stable diffusion, midjourney and dall-e 2. *arXiv preprint arXiv:2210.00586*.

Cao, Y.; Li, S.; Liu, Y.; Yan, Z.; Dai, Y.; Yu, P. S.; and Sun, L. 2023. A comprehensive survey of ai-generated content (aigc): A history of generative ai from gan to chatgpt. *arXiv preprint arXiv:2303.04226*.

Chen, J.; Yu, J.; Ge, C.; Yao, L.; Xie, E.; Wang, Z.; Kwok, J. T.; Luo, P.; Lu, H.; and Li, Z. 2024. PixArt- $\alpha$ : Fast Training of Diffusion Transformer for Photorealistic Text-to-Image Synthesis. In *ICLR*.

Cima, L.; Miaschi, A.; Trujillo, A.; Avvenuti, M.; Dell’Orletta, F.; and Cresci, S. 2025. Contextualized counterspeech: Strategies for adaptation, personalization, and evaluation. In *Proceedings of the ACM on Web Conference 2025*, 5022–5033.

Coccomini, D. A.; Caldelli, R.; Gennaro, C.; Fiameni, G.; Amato, G.; and Falchi, F. 2024. Deepfake detection without deepfakes: Generalization via synthetic frequency patterns injection. *arXiv preprint arXiv:2403.13479*.

Ding, M.; Yang, Z.; Hong, W.; Zheng, W.; Zhou, C.; Yin, D.; Lin, J.; Zou, X.; Shao, Z.; Yang, H.; and Tang, J. 2021. CogView: Mastering Text-to-Image Generation via Transformers. In *Advances in Neural Information Processing Systems*, volume 34, 19822–19835.

Esser, P.; Rombach, R.; and Ommer, B. 2021. Taming transformers for high-resolution image synthesis. In *Proceedings of the IEEE/CVF conference on computer vision and pattern recognition*, 12873–12883.

Fernandez, P.; Couairon, G.; Jégou, H.; Douze, M.; and Furion, T. 2023. The stable signature: Rooting watermarks in latent diffusion models. In *Proceedings of the IEEE/CVF International Conference on Computer Vision*, 22466–22477.

Giorgi, T.; Cima, L.; Fagni, T.; Avvenuti, M.; and Cresci, S. 2025. Human and LLM biases in hate speech annotations: A socio-demographic analysis of annotators and targets. In *Proceedings of the International AAAI Conference on Web and Social Media*, volume 19, 653–670.

Ho, J.; Jain, A.; and Abbeel, P. 2020. Denoising diffusion probabilistic models. *Advances in neural information processing systems*, 33: 6840–6851.

Jiang, X.; and Tian, J. 2024. Source Attribution for Images Generated by Diffusion-Based Text-to-Image Models: Exploring the Forensics Approach. In *2024 Asia Pacific Signal and Information Processing Association Annual Summit and Conference (APSIPA ASC)*, 1–6. IEEE.

Karageorgiou, D.; Papadopoulos, S.; Kompatsiaris, I.; and Gavves, E. 2025. Any-resolution ai-generated image detection by spectral learning. In *Proceedings of the Computer Vision and Pattern Recognition Conference*, 18706–18717.

Keita, M.; Hamidouche, W.; Eutamene, H. B.; Taleb-Ahmed, A.; and Hadid, A. 2025. FIDAVL: Fake Image Detection and Attribution Using Vision-Language Model. In *International Conference on Pattern Recognition*, 160–176. Springer.

Kim, C.; Min, K.; Patel, M.; Cheng, S.; and Yang, Y. 2024. Wouaf: Weight modulation for user attribution and fingerprinting in text-to-image diffusion models. In *Proceedings of the IEEE/CVF Conference on Computer Vision and Pattern Recognition*, 8974–8983.

Kirchenbauer, J.; Geiping, J.; Wen, Y.; Katz, J.; Miers, I.; and Goldstein, T. 2023. A watermark for large language models. In *International Conference on Machine Learning*, 17061–17084. PMLR.

Li, J.; Wang, H.; Li, S.; Qian, Z.; Zhang, X.; and Vasilakos, A. V. 2024. Are handcrafted filters helpful for attributing AI-generated images? In *Proceedings of the 32nd ACM International Conference on Multimedia*, 10698–10706.

Li, M.; Xu, R.; Wang, S.; Zhou, L.; Lin, X.; Zhu, C.; Zeng, M.; Ji, H.; and Chang, S.-F. 2022. Clip-event: Connecting text and images with event structures. In *Proceedings of the IEEE/CVF conference on computer vision and pattern recognition*, 16420–16429.

Li, O.; Cai, J.; Hao, Y.; Jiang, X.; Hu, Y.; and Feng, F. 2025. Improving synthetic image detection towards generalization: An image transformation perspective. In *Proceedings of the 31st ACM SIGKDD Conference on Knowledge Discovery and Data Mining V. 1*, 2405–2414.

Liu, X.; Gong, C.; Wu, L.; Zhang, S.; Su, H.; and Liu, Q. 2021. Fusedream: Training-free text-to-image generation with improved clip+ gan space optimization. *arXiv preprint arXiv:2112.01573*.

Marra, F.; Gragnaniello, D.; Verdoliva, L.; and Poggi, G. 2019. Do gans leave artificial fingerprints? In *2019 IEEE conference on multimedia information processing and retrieval (MIPR)*, 506–511. IEEE.

Namani, Y.; Reghioua, I.; Bendiab, G.; Labiod, M. A.; and Shaeles, S. 2025. DeepGuard: Identification and Attribution of AI-Generated Synthetic Images. *Electronics*, 14(4): 665.

Nasery, A.; Hayase, J.; Brooks, C.; Sheng, P.; Tyagi, H.; Viswanath, P.; and Oh, S. 2025. Scalable Fingerprinting of Large Language Models. *arXiv preprint arXiv:2502.07760*.

Nie, G.; Kim, C.; Yang, Y.; and Ren, Y. 2023. Attributing image generative models using latent fingerprints. In *International Conference on Machine Learning*, 26150–26165. PMLR.

Pasupuleti, R.; Vadapalli, R.; and Mader, C. 2023. Cyber security issues and challenges related to generative ai and chatgpt. In *2023 Tenth International Conference on Social Networks Analysis, Management and Security (SNAMS)*, 1–5. IEEE.

Radford, A.; Kim, J. W.; Hallacy, C.; Ramesh, A.; Goh, G.; Agarwal, S.; Sastry, G.; Askell, A.; Mishkin, P.; Clark, J.; et al. 2021. Learning transferable visual models from natural language supervision. In *International conference on machine learning*, 8748–8763. PMLR.

Ramesh, A.; Dhariwal, P.; Nichol, A.; Chu, C.; and Chen, M. 2022a. DALL-E 2: Hierarchical Text-Conditional Image Generation with CLIP Latents. <https://platform.openai.com/docs/models/dall-e-2>. Accessed: 2025-05-18.

Ramesh, A.; Dhariwal, P.; Nichol, A.; Chu, C.; and Chen, M. 2022b. Hierarchical Text-Conditional Image Generation with CLIP Latents. *arXiv e-prints*, arXiv–2204.

Reed, S.; Akata, Z.; Yan, X.; Logeswaran, L.; Schiele, B.; and Lee, H. 2016. Generative Adversarial Text to Image Synthesis. In *Proceedings of the 33rd International Conference on Machine Learning*, 1060–1069.

Ricco, E.; Cima, L.; and Di Pietro, R. 2025. Hallucination Detection: A Probabilistic Framework Using Embeddings Distance Analysis. *arXiv preprint arXiv:2502.08663*.

Rombach, R.; Blattmann, A.; Lorenz, D.; Esser, P.; and Ommer, B. 2022. High-Resolution Image Synthesis With Latent Diffusion Models. In *Proceedings of the IEEE/CVF Conference on Computer Vision and Pattern Recognition (CVPR)*, 10684–10695.

Sha, Z.; Li, Z.; Yu, N.; and Zhang, Y. 2023. De-fake: Detection and attribution of fake images generated by text-to-image generation models. In *Proceedings of the 2023 ACM SIGSAC conference on computer and communications security*, 3418–3432.

Sha, Z.; Tan, Y.; Li, M.; Backes, M.; and Zhang, Y. 2024. ZeroFake: Zero-Shot Detection of Fake Images Generated and Edited by Text-to-Image Generation Models. In *Proceedings of the 2024 on ACM SIGSAC Conference on Computer and Communications Security*, 4852–4866.

Tan, C.; Zhao, Y.; Wei, S.; Gu, G.; Liu, P.; and Wei, Y. 2024. Frequency-aware deepfake detection: Improving generalizability through frequency space domain learning. In *Proceedings of the AAAI Conference on Artificial Intelligence*, volume 38, 5052–5060.

Wang, Z.; Chen, C.; Zeng, Y.; Lyu, L.; and Ma, S. 2023. Where did i come from? origin attribution of ai-generated images. *Advances in neural information processing systems*, 36: 74478–74500.

Wanli, P.; Yiming, X.; et al. 2025. ImF: Implicit Fingerprint for Large Language Models. *arXiv preprint arXiv:2503.21805*.

Wen, Y.; Kirchenbauer, J.; Geiping, J.; and Goldstein, T. 2023. Tree-rings watermarks: Invisible fingerprints for diffusion images. *Advances in Neural Information Processing Systems*, 36: 58047–58063.

Wißmann, A.; Zeiler, S.; Nickel, R. M.; and Kolossa, D. 2024. Whodunit: Detection and Attribution of Synthetic Images by Leveraging Model-specific Fingerprints. In *Proceedings of the 3rd ACM International Workshop on Multimedia AI against Disinformation*, 65–72.

Xie, E.; Chen, J.; Chen, J.; Cai, H.; Tang, H.; Lin, Y.; Zhang, Z.; Li, M.; Zhu, L.; Lu, Y.; and Han, S. 2024. Sana: Efficient High-Resolution Image Synthesis with Linear Diffusion Transformer. *arXiv:2410.10629*.

Xu, J.; Wang, F.; Ma, M.; Koh, P. W.; Xiao, C.; and Chen, M. 2024. Instructional Fingerprinting of Large Language Models. In *Proceedings of the 2024 Conference of the North American Chapter of the Association for Computational Linguistics: Human Language Technologies (Volume 1: Long Papers)*, 3277–3306.

Xu, K.; Zhang, L.; and Shi, J. 2025. Detecting Origin Attribution for Text-to-Image Diffusion Models. In *2025 IEEE/CVF Winter Conference on Applications of Computer Vision (WACV)*, 8775–8785. IEEE.

Yamabe, S.; Takahashi, T.; Waseda, F.; and Wataoka, K. 2024. MergePrint: Robust Fingerprinting against Merging Large Language Models. *arXiv preprint arXiv:2410.08604*.

Yu, J.; Xu, Y.; Koh, J. Y.; Luong, T.; Baid, G.; Wang, Z.; Vasudevan, V.; Ku, A.; Yang, Y.; Ayan, B. K.; et al. 2022. Scaling Autoregressive Models for Content-Rich Text-to-Image Generation. *arXiv preprint arXiv:2206.10789*.

Yu, N.; Davis, L. S.; and Fritz, M. 2019. Attributing fake images to gans: Learning and analyzing gan fingerprints. In *Proceedings of the IEEE/CVF international conference on computer vision*, 7556–7566.

Yu, N.; Skripniuk, V.; Abdehnabi, S.; and Fritz, M. 2021. Artificial fingerprinting for generative models: Rooting deepfake attribution in training data. In *Proceedings of the IEEE/CVF International conference on computer vision*, 14448–14457.

Zeng, B.; Wang, L.; Hu, Y.; Xu, Y.; Zhou, C.; Wang, X.; Yu, Y.; and Lin, Z. 2024. Huref: Human-readable fingerprint for large language models. *Advances in Neural Information Processing Systems*, 37: 126332–126362.

Zhan, F.; Yu, Y.; Wu, R.; Zhang, J.; Lu, S.; Liu, L.; Kotylewski, A.; Theobalt, C.; and Xing, E. 2023. Multimodal image synthesis and editing: The generative AI era. *IEEE Transactions on Pattern Analysis and Machine Intelligence*, 45(12): 15098–15119.

Zhao, S.; Zhang, B.; Yang, J.; Zhou, J.; and Xu, Y. 2024. Linear discriminant analysis. *Nature Reviews Methods Primers*, 4(1): 70.

Zhong, X.; Dasgupta, A.; and Tanvir, A. 2024. Watermarking Language Models through Language Models. *arXiv preprint arXiv:2411.05091*.

Zhu, M.; Chen, H.; Yan, Q.; Huang, X.; Lin, G.; Li, W.; Tu, Z.; Hu, H.; Hu, J.; and Wang, Y. 2023. Genimage: A million-scale benchmark for detecting ai-generated image. *Advances in Neural Information Processing Systems*, 36: 77771–77782.

## A Comparative Charts

The interested reader can find a comparison chart of the various works involving multi-class attribution of AI-generated images in Table 3.

Also, Table 4 present a comparison chart of the literature datasets of generated image compared to our proposed PRISM-36K.

Finally, Table 5 presents the details of the six T2I models used to generate the PRISM-36K.

## B Prompts

For the sake of completeness, we report in what follows the short and long prompts used to generate the PRISM-36K dataset.

### *Short prompts:*

1. A cat lying on the table
2. A dog running on grass
3. A man walking on sand
4. An astronaut flying into space
5. A girl swimming in the sea
6. An apple in a fruit bowl
7. A starred night in the dark
8. A sailboat in the stormy sea
9. A bird perched on a tree
10. A scene from War and Peace
11. A butterfly landing on a flower
12. A child playing in the snow
13. A chef cooking in a kitchen
14. A car driving through mountains
15. A painter working on a canvas
16. A wave crashing against rocks
17. A robot building a structure
18. A fox hiding in bushes
19. A balloon floating in the sky
20. A writer typing on a laptop

### *Long prompts:*

21. A cat lying on the table while its owner throws it a yellow and red ball to play with
22. A dog running across the grass towards a child waiting for him with open arms
23. A man walking on the beach with his son on the shore of a stormy sea with a purple kite
24. An astronaut flying in space observing Planet Earth from black space in his white suit
25. A girl swimming in the sea with curly blond hair next to a white sailboat with a black hull
26. An apple in a fruit bowl during a huge sandstorm in the red Sahara desert near a waterhole

27. A starred night in the dark as a shining comet passes by with a vortex of lightning stars
28. A sailboat in the stormy sea under a black hole with flying fairies playing classical music
29. A bird perched on a tree with code flowing through its branches with a clock showing 12 am
30. A scene from War and Peace reinterpreted in a futuristic landscape with robots instead of humans
31. A butterfly landing on a flower while a photographer tries to capture the moment
32. A child playing in the snow with red mittens while building an ice castle that glows with blue light
33. A chef cooking in a kitchen filled with steam as magical ingredients float in the air
34. A car driving through mountains on a winding road with colorful autumn leaves swirling around
35. A painter working on a canvas while the subjects of the painting step into the real world
36. A wave crashing against rocks revealing an ancient underwater city with merfolk observers
37. A robot building a structure made of translucent crystals on the surface of Mars
38. A fox hiding in bushes with a pocket watch around its neck as it waits for the perfect moment
39. A balloon floating in the sky carrying a tiny house with a chimney that releases rainbow smoke
40. A writer typing on a laptop beside a window showing different dimensions with each keystroke

## C DFT and Radial Aggregation

In what follows, we discuss in detail the feature extraction procedure adopted in Section 4.1.

Given an input image with resolution  $n_x \times n_y$  and pixel values in  $\mathbb{N}_{256}$ , we consider each colour channel independently. Let  $I \in \mathbb{N}_{256}^{n_y \times n_x}$  denote one such channel (in the case of our PRISM-36K,  $n_x = n_y = 512$ ). The two-dimensional Discrete Fourier Transform (DFT) of  $I$  is the complex-valued matrix  $\widehat{I} \in \mathbb{C}^{n_y \times n_x}$  defined by:

$$\widehat{I}_{u,v} = \sum_{x=0}^{n_x-1} \sum_{y=0}^{n_y-1} I_{x,y} e^{-2\pi i \left( \frac{ux}{n_x} + \frac{vy}{n_y} \right)}, \quad (5)$$

where each entry  $\widehat{I}_{u,v}$  encodes the amplitude and phase of a spatial frequency component as the magnitude and angle of the complex value.

To facilitate interpretation, we perform a standard frequency centralisation by shifting the zero-frequency component (DC component) to the centre of the matrix. This is done via a two-dimensional circular shift:

$$\tilde{I}_{u,v} = \widehat{I}_{(u+n_x/2) \bmod n_x, (v+n_y/2) \bmod n_y}, \quad (6)$$

Table 3: Overview of the different approaches to multi-class fingerprinting AI-generated images.

Paper	Task	Feature Extraction	Model	Learning	Dataset
DE-FAKE (Sha et al. 2023)	Real vs fake detection	Average Fourier Transform	CNN	Supervised	MSCOCO Flickr30k
AI Attribution (Wang et al. 2023)	Origin Attribution	Reverse engineering	Optimisation Algorithm	Supervised	CIFAR-10 ImageNet CUB-200-2011
Whodunit (Wißmann et al. 2024)	Image Fingerprinting	Discrete Cosine Transform Power Spectral Density	ResNet50	Supervised	CelebA Diffusion Models*
Handcrafted Filters (Li et al. 2024)	Origin Attribution	Multi-Directional High-Pass Filters	ResNet50	Supervised	GAN Diffusion Models* ImageNet
Forensics Approach (Jiang and Tian 2024)	Origin Attribution	CLIP, HR-NET	Supervised Contrastative Loss	Supervised	Diffusion Models* MS-COCO
FIDAVL (Keita et al. 2025)	Origin Attribution	Image Encoder	Q-Former	Supervised	GAN Diffusion Models*
DeepGuard (Namani et al. 2025)	Origin Attribution	Binary Classifier	Ensemble Learning	Supervised	DeepGuardDB
Detect Origin (Xu, Zhang, and Shi 2025)	Origin Attribution	Style features (Gram matrices), RGB	EfficientFormer	Supervised	Diffusion Models* MS-COCO
<b>PRISM</b> ( <i>Ours</i> )	Image Fingerprinting	Radial DFT	K-Means	Unsupervised	PRISM-36K
			Fuzzy-C-Means		GFW
			GMM		DeepGuardDB
			LDA	Supervised	SuSy GenImage

\*Diffusion Models denotes a subset of LDM, Glide, ADM, Stable Diffusion v1.4, VQDM, DALL-E 2, and Midjourney. Details are in the cited papers.

Table 4: Comparison of our dataset with other reference datasets.

Reference	Dimension	Format	Ref. Split	Models			
				Name	Resolution	Dimension	Classes
GFW (Borji 2022)	76,000	.jpeg	✗	DALL-E 2	100 × 100, 512 × 512	1,109	Faces, Images
				Midjourney	100 × 100, various	18,609	Faces, Images
				Stable Diffusion v1.4	100 × 100, 512 × 512	26,282	Faces, Images
				Real Faces*	100 × 100	30,000	Faces
GenImage (Zhu et al. 2023) ( <i>Tiny</i> )	35,000	.jpeg .png	✓	Nature*	various	17,500	Real
				ADM	256 × 256	2,500	Fake
				BiGAN	128 × 128	2,500	Fake
				GLIDE	256 × 256	2,500	Fake
				Midjourney	1024 × 1024	2,500	Fake
				Stable Diffusion v1.5	512 × 512	2,500	Fake
				VQDM	256 × 256	2,500	Fake
				Wukong	512 × 512	2,500	Fake
SuSy (Bernabeu-Perez, Lopez-Cuena, and Garcia-Gasulla 2024)	20,004	.jpeg .png	✓	COCO	various	4,201	Real*
				DALL-E 3	various	1,317	Fake
				Stable Diffusion v1.X	512 × 512	4,200	Fake
				SDXL	various	4,201	Fake
				Midjourney-tti	1024 × 1024	3,624	Fake
				Midjourney-img	1024 × 1024	2,461	Fake
DeepGuardDB (Namani et al. 2025)	13,000	.png .jpeg .webp (lossy)	✗	Real		6,500	Real
				DALL-E 3		2,150	Fake
				Stable Diffusion v3.0		2,675	Fake
				GLIDE		500	Fake
				IMAGEN		1,175	Fake
<b>PRISM-36K</b> ( <i>Ours</i> )	36,000	.png	✓	DALL-E 2		6,000	
				FuseDream		6,000	
				PIXART- $\alpha$		6,000	
				SANA		6,000	
				Stable Diffusion v1.4		6,000	
				VQGAN-CLIP		6,000	20 long prompts & 20 short prompts

Table 5: Details of the T2I models used to generate the PRISM-36K dataset.

Model	Reference	Resolution	Architecture		Openness
			GAN+CLIP	Transformers+Diffusion	
VQGAN-CLIP	(Esser, Rombach, and Ommer 2021) (Li et al. 2022)	Custom*	✓		Partially Open
Stable Diffusion v1.4	(Rombach et al. 2022)	512 × 512		✓	Fully Open
SANA	(Xie et al. 2024)	Custom*		✓	Partially Open
PIXART- $\alpha$	(Chen et al. 2024)	Custom*		✓	Partially Open
FuseDream	(Liu et al. 2021)	256 × 256, 512 × 512	✓		Partially Open
DALL-E 2	(Ramesh et al. 2022b)	256 × 256, 512 × 512, 1024 × 1024		✓	Closed

\*Custom refers to the possibility for the user to decide the resolution.

so that lower frequencies are positioned at the centre of the spectrum, with higher frequencies distributed symmetrically outward.

From the centralised spectrum  $\tilde{I}$ , we extract:

$$\overline{M}_{u,v} = \log \left( \left| \tilde{I}_{u,v} \right| + 1 \right), \quad \overline{\Phi}_{u,v} = \arg(\tilde{I}_{u,v}), \quad (7)$$

representing the log-scaled magnitude and phase at frequency  $(u, v)$ . The log-scaling improves numerical stability and compresses dynamic range.

To obtain a compact and dimension-agnostic descriptor, we compute a radial DFT profile (rDFT). This aggregates spectral information across annular frequency regions. Specifically, for each frequency index  $(u, v)$ , we compute its Euclidean distance from the centre:

$$r(u, v) = \left\| (u, v) - (n_x/2, n_y/2) \right\|_2, \quad (8)$$

and assign it to one of  $n_r = 64$  evenly spaced radial bins  $\mathcal{B}_1, \dots, \mathcal{B}_{n_r}$  covering the full frequency range.

Then, for each bin  $i = 1, \dots, n_r$ , we define the aggregated log-magnitude and phase as in (2) and (3) we here report for completeness:

$$M_i = \frac{1}{|\mathcal{B}_i|} \sum_{(u,v) \in \mathcal{B}_i} \overline{M}_{u,v}, \quad (9)$$

$$\Phi_i = \cos \left( \arg \left( \frac{1}{|\mathcal{B}_i|} \sum_{(u,v) \in \mathcal{B}_i} (u, v) \in \mathcal{B}_i e^{i \overline{\Phi}_{u,v}} \right) \right), \quad (10)$$

where  $\arg(\cdot)$  denotes the complex argument and the outer cosine transform is used to identify  $\pm\pi$  by collapsing opposite directions (*i.e.*  $0 \pm \epsilon$  and  $\pm\pi \mp \epsilon$ ) onto a consistent representation. This is especially justified by the Hermitian property of the DFT (due to the real-valued input), which ensures phase symmetry and supports this form of aggregation, yet potentially being subject to numerical issues  $\epsilon \neq 0$ .

The result is a fixed-size, rotation-invariant vector that captures the spectral distribution of both amplitude and phase across radial frequency bands. This transformation also promotes robustness to variations in image resolution and compression artefacts.